Capacitive Micromachined Ultrasonic Transducer Design for High Power Transmission

Baris Bayram, *Student Member, IEEE*, Ömer Oralkan, *Member, IEEE*, A. Sanli Ergun, *Member, IEEE*, Edward Hæggström, Goksen G. Yaralioglu, *Member, IEEE*, and Butrus T. Khuri-Yakub, *Fellow, IEEE*

***Abstract*—Capacitive micromachined ultrasonic transducers (cMUTs) were developed to meet the demands of the ultrasonic industry. To achieve maximum efficiency, the conventional operation of the cMUT requires a bias voltage close to the collapse voltage. Total acoustic output pressure is limited by the efficiency of the cMUT and the maximum-allowed pulse voltage on the membrane. In this paper, we propose the collapse-snapback operation of the cMUT: the membrane is collapsed onto the substrate in the collapsing cycle, and released in the snapback cycle. The collapse-snapback operation overcomes the above-mentioned limitations of the conventional operation. The collapse-snapback operation utilizes a larger range of membrane deflection profiles (both collapsed and released profiles) and generates higher acoustic output pressures. The static finite element calculations were performed to design cMUTs with specific collapse and snapback voltages by changing the electrode parameters (radius (r_e), position (d_e), and thickness (t_e)). These designs were refined for optimum average displacement per cycle. An electrode radius greater than 60% of the membrane radius significantly improved the displacement per volt. Moderately thick membranes ($t_e \sim 0.2$ μm) were preferred, as thicker membranes reduced the displacement per volt. Under proper bias conditions, the collapse-snapback operation, designed for high-power transmission, allowed the application of pulse voltages larger than the difference of collapse and snapback voltages. Dynamic finite element calculations of an infinite cMUT array on the substrate loaded with acoustic fluid medium were performed to determine the dynamic response of the cMUT. Commercially available FEM packages ANSYS and LS-DYNA were used for static and dynamic calculations, respectively. The cMUTs were fabricated for optimal performance in the collapse-snapback operation. The transmit experiments were performed on a 2-D cMUT array using a calibrated hydrophone. Taking into account the attenuation and diffraction losses, the pressure on the cMUT surface was extracted. The cMUT generated 0.47 MPa (6 kPa/V) and 1.04 MPa (11 kPa/V) in the conventional and collapse-snapback operations, respectively. Therefore, collapse-snapback operation of the cMUTs was superior for high-power transmission.**

I. Introduction

Capacitive micromachined ultrasonic transducers (cMUTs) emerged as an alternative to piezoelectric transducers in ultrasonic applications [1]–[4]. cMUTs offered several advantages, such as wide bandwidth, high sensitivity, and ease of fabrication [4]. Recently, cMUTs overcame the difficulties in the realization of 2-D arrays for real-time 3-D imaging [5]. Three-dimensional ultrasound imaging used a 2-D transducer array, which enabled features such as electronic focusing and beam steering in both azimuthal and elevational directions [6], [7]. These features enabled uniform resolution in both azimuthal and elevational directions in addition to accelerating the data acquisition for real-time imaging. One major difficulty of 3-D ultrasound imaging using 2-D cMUTs was the element size restriction due to the spatial sampling criterion [5]. The spatial sampling criterion specifies that the maximum element width must be less than half the acoustic wavelength at the operating frequency in order to prevent grating lobes from appearing in the image. This criterion applies to the directions in which beams are to be steered. Since the 2-D arrays focus and steer beams in both azimuthal and elevational directions, the sampling criterion applies to both dimensions of the array and critically limits the element area, causing degradation in the acoustic output power. The acoustic output power degradation becomes even more severe in high-frequency ultrasound. This paper introduces the collapse-snapback operation regime for the cMUTs as a way to boost the acoustic output pressure, making the 2-D arrays' performance satisfactory for high-frequency 3-D ultrasound imaging.

Finite element methods (FEM) and analytical models were developed to improve the performance of the cMUT [8]–[18]. All of these analyses were focused on understanding and optimizing the cMUT behavior in the conventional operation regime, where the membrane and the substrate do not touch each other. Recently, a new operation regime, collapsed operation, was proposed for the cMUTs [19]. Based on static FEM calculations, the collapsed operation regime provided coupling efficiency (k_T^2) greater than 0.7 when the cMUT was initially collapsed by applying a voltage higher than the collapse voltage and then biased between collapse and snapback voltages [19]. Experimental characterization of cMUTs operating in the collapsed regime verified the FEM calculations [20].

Dynamic FEM calculations of a water-loaded single cMUT cell provided important insight into the cMUT dynamics in this nonlinear operation [21]. The collapsed operation had a center frequency of approximately twice the

Manuscript received August 9, 2002; accepted August 20, 2004. This work was supported by the Office of Naval Research. Dr. Hæggström acknowledges the Wihuri-foundation and the Academy of Finland for financial support.

The authors are with the Edward L. Ginzton Laboratory, Stanford University, Stanford, CA 94305-4088 (e-mail: bbayram@stanford.edu).

0885–3010/$20.00 © 2005 IEEE

natural frequency of the conventional operation. A major breakthrough toward low-voltage, high-frequency cMUT designs [21] was realized in the additional center-frequency tunability of the cMUT by adjusting the bias voltage in the collapsed state. Collapsed operation assumed that the applied voltage was larger than the snapback voltage to keep the center of the membrane in contact with the substrate. This operation was proposed to provide higher acoustic output pressure per volt from small voltage excitations (5% of the collapse voltage) up to moderately large voltage excitations (50% of the collapse voltage) limited by the breakdown voltage [21]. However, neither conventional nor collapsed operation regimes took full advantage of the inherent cMUT potential: the collapse-snapback operation combines two distinct states of the membrane (in-collapse and out-of-collapse) to unleash unprecedented acoustic output pressures into the medium [21].

When the total applied voltage exceeded the collapse voltage, the collapse of the membrane resulted in large membrane displacement. However, in order to restore the collapsed membrane to its pre-collapsed state, the applied voltage was decreased below the snapback voltage of the device [19]. Snapback of the membrane resulted in a large membrane displacement as well. Therefore, the collapse-snapback cycle utilized the inherent membrane displacement potential in collapse and snapback of the membrane, which translated into high transmit power for the cMUT. Collapse and snapback voltages are the static parameters, determining the membrane displacement change in this nonlinear operation. However, an additional important parameter was demonstrated by the dynamic response of the membrane to collapse or the already collapsed membrane to snapback: the collapse and snapback times determined the switching of the membrane state between in-collapse and out-of-collapse [22]. Therefore, dynamic FEM calculations of infinite-size cMUT were used to determine the dynamic response of the cMUT [22]. The static FEM calculations of net membrane displacement combined with the dynamic FEM calculations of transition times between in-collapse and out-of-collapse membrane states fully described the collapse-snapback operation. Finally, in order to evaluate the cMUT performance in this operation, experimental characterization of a cMUT was done via transmit experiments, performed on a 2-D cMUT array using a calibrated hydrophone. Taking into account the attenuation and diffraction losses, the pressure on the cMUT surface was extracted. The cMUT generated 0.47 MPa (6 kPa/V) and 1.04 MPa (11 kPa/V) in the conventional and collapse-snapback operations, respectively. Therefore, collapse-snapback operation of the cMUTs was shown again to be superior for high-power transmission.

This paper presents the cMUT design for the collapse-snapback operation. Operating the cMUT in a collapse-snapback cycle generates greater output pressures than does the conventional operation, and solves the limited acoustic power capability of 2-D cMUT elements operated conventionally. Therefore, high-frequency ultrasound imaging systems using 2-D cMUT arrays will deliver greater acoustic output pressures in the collapse-snapback operation.

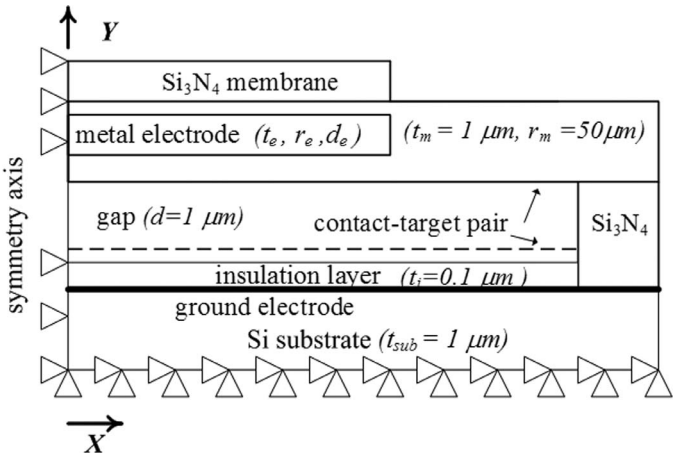

Fig. 1. The cMUT model, where t_e, r_e, and d_e are the thickness, the radius, and the position of the metal electrode, respectively.

II. Finite Element Calculations

Capacitive micromachined ultrasonic transducers are fabricated using surface micromachining or wafer-bonding technique [23]–[25]. Surface micromachined ultrasonic transducers use silicon nitride (Si_3N_4) as both membrane and insulation layer material [23]. Wafer-bonded ultrasonic transducers use silicon as membrane and silicon oxide (SiO_2) as insulation layer material [25]. In this study, static finite element calculations for the influence of electrode parameters on the collapse and snapback voltages assumed silicon nitride in both membrane and insulation layer in the model. However, since the experimental results were measured using a wafer-bonded cMUT array, the static and dynamic finite element calculations of this cMUT required modeling with silicon membrane and silicon oxide (SiO_2) insulation layer.

To determine the influence of electrode parameters on collapse and snapback voltages, a circular cMUT cell was modeled, which featured a circular silicon nitride (Si_3N_4) membrane. A vacuum gap separated the substrate from the membrane supported at its rim. A thin insulation layer of Si_3N_4 over the highly doped silicon (Si) substrate prevented short circuit in collapse.

The static finite element calculations of the cMUT were performed using a commercially available FEM package (ANSYS 5.7) [26]. The cMUT model is shown schematically in Fig. 1. The axisymmetric structure allowed the use of 2D modeling. In the structural analysis, the symmetry axis of the model was clamped in the x-direction, and the substrate was supported at the bottom (Fig. 1). The infinitesimally thick ground electrode was located on the top surface of the silicon substrate. The other electrode, made of aluminum (Al), was an integral part of the membrane. Electrode dimensions were defined as the radius (r_e) and

TABLE I
PROPERTIES OF THE MATERIALS USED IN THE FINITE ELEMENT CALCULATIONS.

	Si_3N_4	Si	SiO_2	Al	Vacuum	Water
Young's modulus (GPa)	320	169	75	67.6		
Density (kg/m^3)	3270	2332	2200	2700		1000
Poisson's ratio	0.263	0.290	0.170	0.355		
Relative permittivity	5.7	11.8	3.78		1	
Velocity of sound (m/s)						1500

the thickness (t_e). The electrode was circular and coaxial with the membrane. The vertical distance (d_e) between the bottom of the Si_3N_4 membrane and the metal electrode determined the electrode position. The Si_3N_4 membrane thickness and gap height were both 1 μm. The circular cMUT had a 50-μm radius for the active membrane. The Si_3N_4 insulation layer was 0.1 μm. In order to model the membrane substrate contact, FEM elements were defined on the contacting surfaces as described in the following paragraph.

ANSYS standard element type PLANE121, which featured charge and voltage variables, and PLANE82, which featured displacement and force variables, were used for electrostatic and structural analyses, respectively [26]. The collapse of the membrane onto the substrate was modeled by means of contact-target pair elements (CONTA172 and TARGE169) [26]. These surface elements detected contact between the surfaces and automatically applied the resulting contact forces. When contact occurred, the penetration of the surfaces and the forces due to the contact were calculated based on the material properties of Si_3N_4 used in the contacting surfaces of the membrane and the insulation layer. The surface elements were defined on both the bottom surface of the membrane and slightly above the insulation layer. The offset from the insulation layer, which was included to re-mesh the gap when the structure was collapsed, was 5% of the gap in the analysis.

FEM was used to calculate the deflected membrane profile for applied bias voltage. The electrostatic-structural coupled solver, ESSOLV of ANSYS, was used to iterate automatically between the electrostatic and structural domains until the convergence criterion (based on both the electrostatic energy and the maximum structural displacement in the model) was met [26]. Collapse and snapback voltages were calculated with a relative error bound of 1%. A membrane under greater than the collapse voltage, collapsed: an already collapsed membrane, under smaller than the snapback voltage, snapped back from the substrate.

The cMUTs used in the experiments were hexagonal in shape. However, they were modeled with square shapes in the static and dynamic finite element calculations. Therefore, the above-mentioned 2-D axisymmetric model was modified for a square membrane modeled in 3-D. In the dynamic finite element calculations, the commercially available FEM package LS-DYNA was used, due to the availability of enhanced contact capabilities and an explicit time domain solver [27]. The details of this finite element analysis will be found in [22]. The physical dimensions of the square cMUT, used in the finite element calculations and the experiments, are given in Section III.

The structural and electrical material properties used in the FEM calculations are presented in Table I. The only material parameter required for the electrostatic analysis was the dielectric constant. The structural analysis used Young's modulus, density, and Poisson's ratio. Since the membrane was water-loaded, the dynamic FEM calculations additionally used the density and velocity of the acoustic medium.

III. RESULTS

Membrane deflection profiles of the cMUT about collapse and snapback voltages are depicted in Fig. 2(a). The infinitesimally thick electrode ($t_e = 0$ μm) was positioned on the top of the membrane ($d_e = 1$ μm). The electrode radius was half of the membrane radius ($r'_e = r_e/R = 0.5$). The collapse and snapback voltages were 177 V and 140 V, respectively. The range of the membrane deflection profile [Fig. 2(a)] is well defined in the conventional ("1") and collapsed ("2") operation regimes for applied voltages limited by the collapse and snapback voltages of the cMUT. However, the profiles at the collapse and snapback voltages were unstable; therefore, a slight voltage change above the collapse or below the snapback voltage caused the membrane to collapse, or the already collapsed membrane to snapback, respectively. The range of the membrane profile in the collapse-snapback operation ("3") was greater than the total range of the conventional and collapsed operation regimes combined. In the static analysis, there was no additional voltage required for the cMUT in the conventional ("1") or collapsed ("2") operation to switch to the collapse-snapback ("3") operation in the limit.

The average and maximum membrane displacements ($r'_e = 0.5$, $d_e = 1$ μm) are depicted in Fig. 2(b). The net average displacement between the collapse and snapback voltages was 799 Å (22 Å/V) in the conventional ("1") and 524 Å (14 Å/V) in the collapsed ("2") operation regimes. The collapse-snapback operation yielded 2873 Å (70 Å/V) net average displacement. The displacement per volt of the cMUT was almost twice as large in the collapse-snapback operation as in the conventional and collapsed operations summed together.

In the collapse-snapback operation, 70 Å/V average displacement was calculated when the voltages of in-collapse

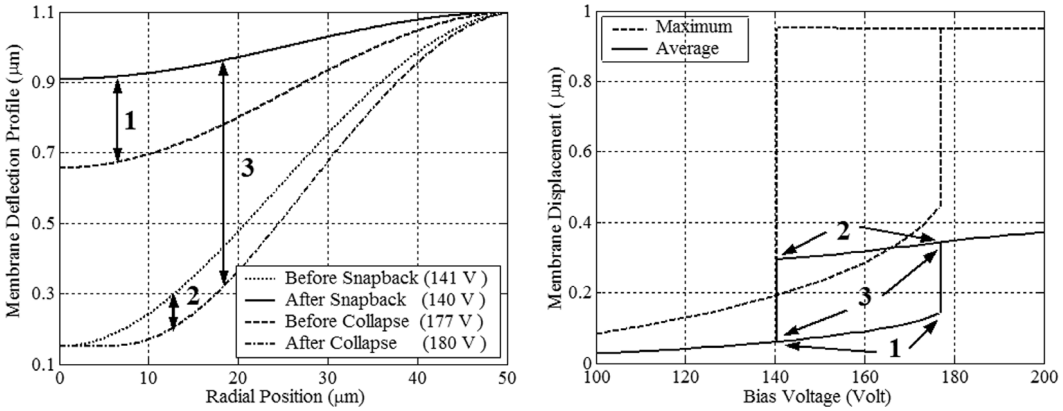

Fig. 2. Operation regimes of the cMUT ($r'_e = 0.5$, $d_e = 1$ μm). The conventional, collapsed, and collapse-snapback operations between collapse and snapback voltages are denoted by "1," "2," and "3," respectively. (a) The membrane deflection profile of the cMUT. The dashed and the dash-dotted lines are just prior to collapse and after collapse, respectively. The dotted and the solid lines are just prior to snapback and after snapback, respectively. (b) Membrane displacement of the cMUT. The solid and dashed lines represent the average and maximum displacements, respectively.

and out-of-collapse were equal to collapse and snapback voltages. If the operation was extended beyond these voltages, each additional volt contributed 22 Å/V and 14 Å/V in the conventional and collapsed regimes, respectively, reducing the displacement per volt below 70 Å/V. Therefore, maximum displacement per volt of the cMUT was achieved between collapse and snapback voltages. The specified voltages set the limit on the total displacement of the cMUT (2873 Å) in one collapse-snapback cycle for peak performance (70 Å/V). Therefore, the cMUT should be designed for specific collapse and snapback voltages to match the target acoustic output pressure (total membrane displacement in one cycle) of the ultrasonic application. In general, the total membrane displacement and the dynamic response of the cMUT in the collapse-snapback cycle determine the total acoustic output pressure. The static parameters of the cMUT (collapse and snapback voltages, and total membrane displacement) were determined by static finite element calculations. These parameters were optimized for above-mentioned criteria by adjusting the electrode parameters (electrode radius, thickness, and position).

The electrode parameters (r_e, d_e, t_e) determined the average membrane displacement and the displacement per volt of the cMUT in the collapse-snapback operation [Figs. 3(a), (b), (c), and (d)]. The displacement per cycle was defined as the difference between the average displacements of just-collapsed and just-snapped-back membranes. The displacement per volt of the cMUT was calculated as the ratio of the displacement per cycle to the difference between collapse and snapback voltages. Collapse and snapback voltages were recalculated for different (r_e, d_e, t_e) combinations in Figs. 3(a), (b), (c), and (d). The displacement per cycle, corresponding to $d_e = 0$ μm and $t_e = 0$ μm, increased linearly with the electrode radius from 3400 Å ($r'_e = 0.2$) to 4500 Å ($r'_e = 0.5$). The displacement per cycle leveled off to 4600 Å at $r'_e = 0.6$, and was unchanged up to full electrode coverage [Fig. 3(a)]. The displacement per cycle, corresponding to $t_e = 0.2$ μm, had similar characteristics. For $t_e = 0.8$ μm, the displacement per cycle increased linearly with the electrode radius from 3400 Å ($r'_e = 0.2$) to 5600 Å ($r'_e = 0.6$), and was unchanged until $r'_e = 0.7$. Then it decreased to 5000 Å at $r'_e = 0.8$, and was unchanged up to full electrode coverage [Fig. 3(a)].

The displacement per volt, corresponding to $d_e = 0$ μm and $t_e = 0$ μm, increased almost linearly from 18 Å/V ($r'_e = 0.2$) to 80 Å/V ($r'_e = 0.7$), and was 82 Å/V up to full electrode coverage [Fig. 3(b)]. Larger electrode thickness reduced the displacement per volt (78 Å/V ($t_e = 0.2$ μm), 67 Å/V ($t_e = 0.5$ μm), and 57 Å/V ($t_e = 0.8$ μm) at full electrode coverage).

The displacement per cycle, corresponding to $d_e = 1$ μm and $t_e = 0$ μm, was within 6% of 2750 Å for the r'_e between 0.2 and 1.0 [Fig. 3(c)]. Larger electrode thickness increased the displacement per cycle (2750 Å ($t_e = 0.2$ μm), 2950 Å ($t_e = 0.5$ μm), and 3100 Å ($t_e = 0.8$ μm) at full electrode coverage).

The displacement per volt, corresponding to $d_e = 1$ μm and $t_e = 0$ μm, increased almost linearly from 22 Å/V ($r'_e = 0.2$) to 90 Å/V ($r'_e = 0.7$), and was about 100 Å/V up to full electrode coverage [Fig. 3(d)]. Larger electrode thickness reduced the displacement per volt (87 Å/V ($t_e = 0.2$ μm), 80 Å/V ($t_e = 0.5$ μm), and 64 Å/V ($t_e = 0.8$ μm) at full electrode coverage).

Collapse and snapback voltages were calculated as a function of electrode radius for electrode positions $d_e = 0$ μm [Fig. 4(a) and (b)] and $d_e = 1$ μm [Figs. 4(c) and(d)]. Collapse voltage increased from 122 V at $r'_e = 1$ to 140 V at $r'_e = 0.5$ for $t_e = 0$ μm and $d_e = 0$ μm [Fig. 4(a)]. Further reduction of r'_e to 0.2 increased collapse voltage to 264 V. Collapse voltages for $t_e = 0$ μm and $t_e = 0.2$ μm were close to each other. However, larger electrode thickness increased the collapse voltage of the cMUT with full electrode coverage by approximately 20 V for each additional 0.3-μm electrode thickness. Electrode thickness was less effective with reduced electrode radius.

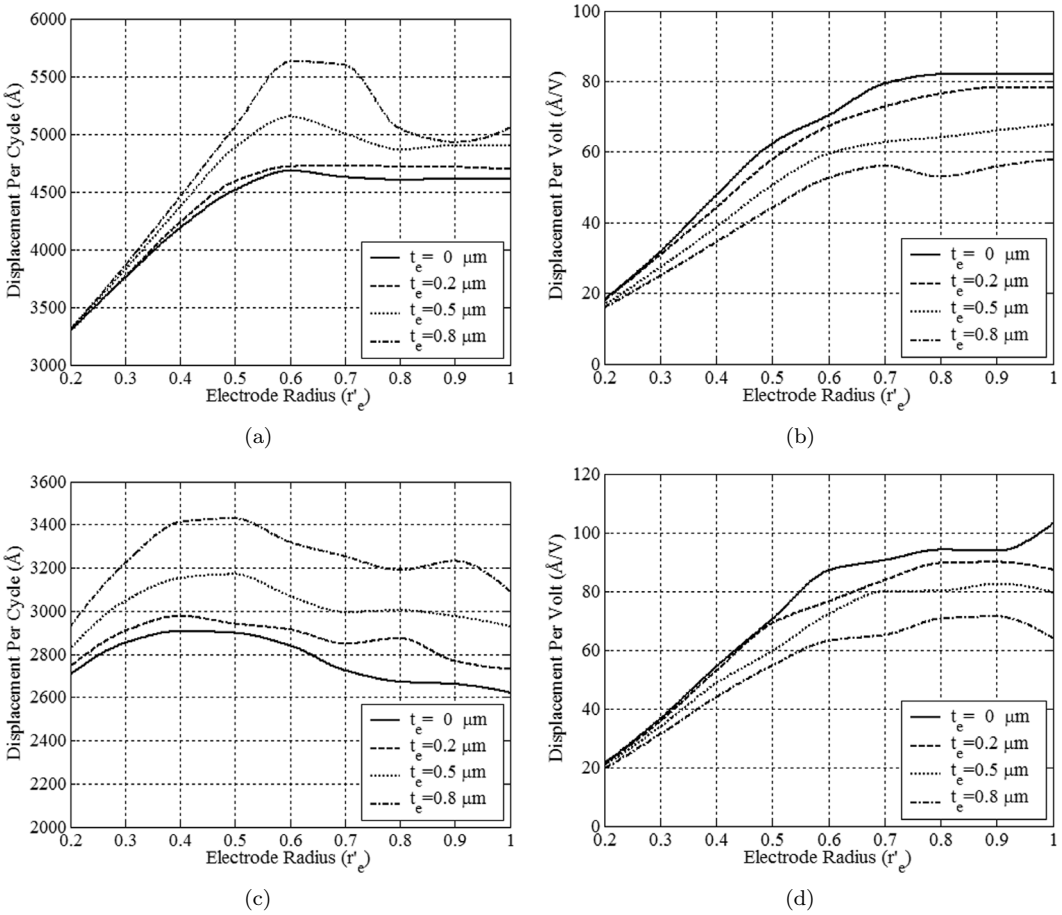

Fig. 3. Displacement per cycle and displacement per volt as a function of electrode radius. The solid, dashed, dotted, and dash-dotted lines represent electrode thicknesses of 0, 0.2, 0.5, and 0.8 μm, respectively. (a) Displacement per cycle-electrode radius curve of the cMUT, $d_e = 0$ μm. (b) Displacement per volt-electrode radius curve of the cMUT, $d_e = 0$ μm. (c) Displacement per cycle-electrode radius curve of the cMUT, $d_e = 1$ μm. (d) Displacement per volt-electrode radius curve of the cMUT, $d_e = 1$ μm.

Snapback voltage ($t_e = 0$ μm and $d_e = 0$ μm) was 66 V for r'_e greater than 0.6 [Fig. 4(b)]. Reducing r'_e to 0.2 increased the snapback voltage to 84 V. Larger electrode thickness reduced the snapback voltage for $r'_e = 0.2$ (81 V ($t_e = 0.2$ μm), 77 V ($t_e = 0.5$ μm), 73 V ($t_e = 0.8$ μm)), but increased the snapback voltage for full electrode coverage (67 V ($t_e = 0.2$ μm), 73 V ($t_e = 0.5$ μm), 83 V ($t_e = 0.8$ μm)).

Collapse and snapback voltages ($d_e = 1$ μm) changed with the electrode radius as depicted in Figs. 4(c) and (d), respectively. The electrode radius influenced the collapse voltage in a similar way for both $d_e = 0$ μm and $d_e = 1$ μm. However, the snapback voltage for $d_e = 1$ μm was consistently larger for thicker electrodes, regardless of the electrode radius. In the snapback-electrode radius curve, the minimum snapback voltage shifted to a smaller electrode radius for larger electrode thickness.

Collapse and snapback voltages ($t_e = 0$ μm) increased linearly from 140 V and 70 V to 180 V and 140 V, respectively, when the electrode position was swept from $d_e = 0$ μm to $d_e = 1$ μm [Figs. 5(a) and (b)]. Large electrode thickness ($t_e = 0.8$ μm) moved the peak collapse voltage to $d_e = 0.7$ μm, whereas the linear relation was still dominant for the snapback voltage. Both collapse and snapback voltages increased for larger electrode thickness.

TABLE II
PHYSICAL DIMENSIONS OF THE 2-D CMUT.

Side length (L) (μm)	32
Membrane thickness (T) (μm)	1.06
Gap thickness (G) (μm)	0.22
Insulating layer thickness (I) (μm)	0.30
Cell periodicity (C) (μm)	38
Substrate (S) (μm)	500

The physical dimensions of the square cMUT are given in Table II. The infinitesimally thick electrode ($t_e = 0$ μm) was at electrode position $d_e = 0$ μm, extending over the entire membrane. The 3-D static finite element results are given in Figs. 6(a) and (b). The calculated collapse and snapback voltages for the cMUT membrane were 130 V and 110 V, respectively. The voltage-capacitance relationship of the cMUT cell is shown in Fig. 6(a). The initial static capacitance of 41.5 fF increased to 47 fF as the bias voltage was increased and came close to the collapse voltage. The collapse of the membrane caused an abrupt increase in the static capacitance to 55 fF. Subsequently,

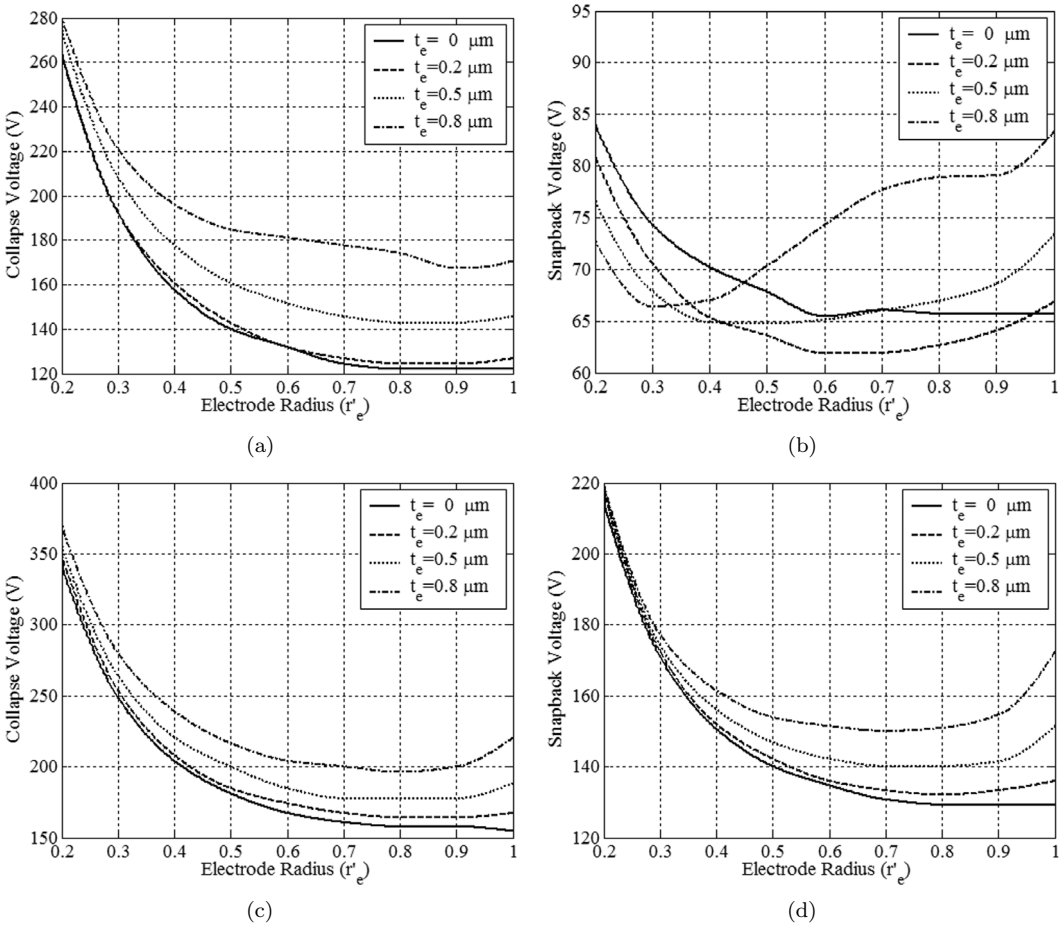

Fig. 4. Collapse and snapback voltages as a function of electrode radius. The solid, dashed, dotted, and dash-dotted lines represent electrode thicknesses of 0, 0.2, 0.5, and 0.8 μm, respectively. (a) Collapse voltage of the cMUT, $d_e = 0$ μm. (b) Snapback voltage of the cMUT, $d_e = 0$ μm. (c) Collapse voltage of the cMUT, $d_e = 1$ μm. (d) Snapback voltage of the cMUT, $d_e = 1$ μm.

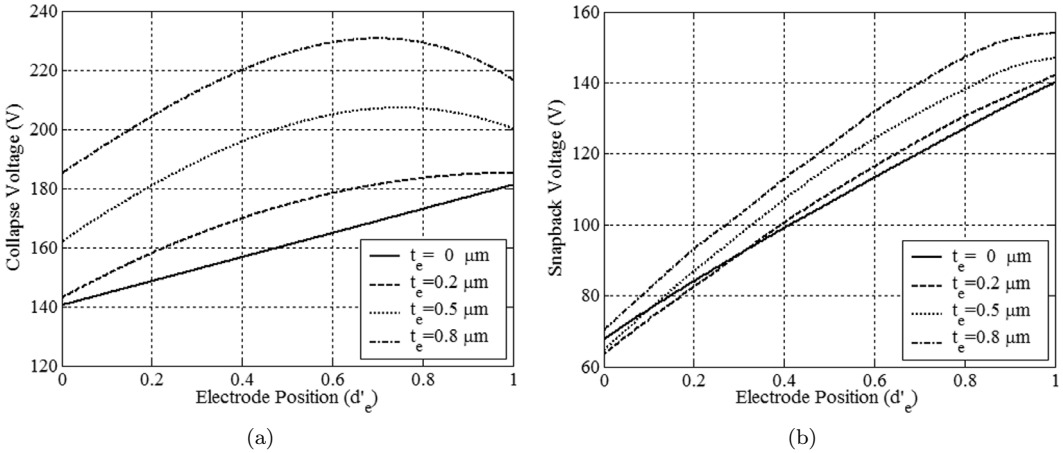

Fig. 5. Collapse and snapback voltages as a function of electrode position. The solid, dashed, dotted, and dash-dotted lines represent electrode thicknesses of 0, 0.2, 0.5, and 0.8 μm, respectively. (a) Collapse voltage of the cMUT, $r'_e = 0.5$. (b) Snapback voltage of the cMUT, $r'_e = 0.5$.

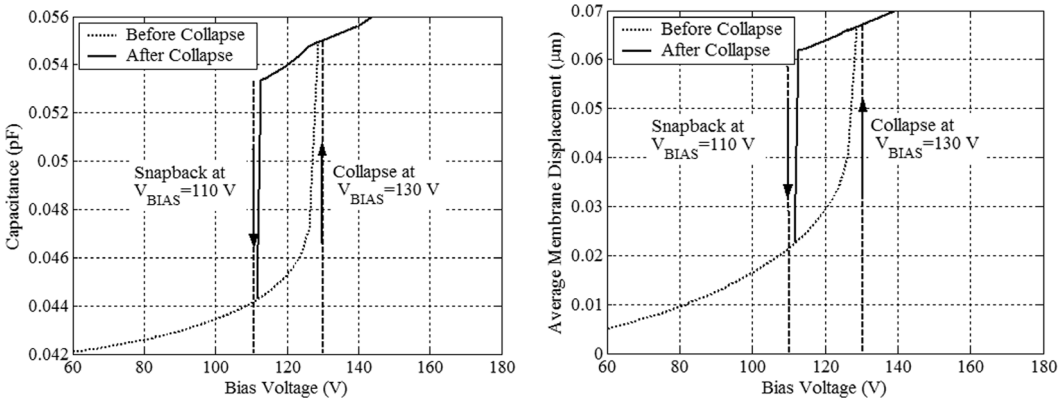

Fig. 6. 3-D static finite element results for a 2-D square cMUT cell. (a) Bias voltage-capacitance curve of the cMUT cell. (b) Bias voltage-average membrane displacement curve of the cMUT cell.

lowering the bias voltage over the collapsed membrane reduced the static capacitance to 53 fF prior to membrane snapback. The static capacitance changed to 44 fF when the membrane snapped back. The voltage-average displacement relationship of the cMUT is given in Fig. 6(b). The average membrane displacement increased from 200 Å at 110 V to 400 Å at a bias voltage close to the collapse voltage (130 V). The collapse of the membrane increased the average displacement to 650 Å. The average displacement decreased to 600 Å prior to membrane snapback. The average displacement was 200 Å for the snapped-back membrane at 110 V.

The static finite element calculations were presented above for the cMUT used in the experiments. A cMUT membrane subject to voltages greater than the collapse voltage will collapse [19]. A collapsed membrane will snap back if the applied voltage is less than the snapback voltage [19]. However, the time that it takes for the membrane to collapse (t_{COLLAPSE}), and the time for a collapsed membrane to snap back (t_{SNAPBACK}) will determine the dynamic response of the cMUT [22]. Therefore, dynamic finite element calculations were used to determine the dynamic response of the cMUT [22]. The average membrane displacement of the cMUT in the collapse-snapback regime is depicted in Fig. 7(a). Initially, the membrane was biased by applying 50 V (60 V below snapback voltage) under atmospheric pressure. The average membrane displacement was -67 Å. At $t = 1$ μs, the voltage was changed to 140 V (10 V above collapse voltage). The time response of average membrane displacement crossed the static membrane displacement value of -820 Å at $t = 1.120$ μs. The collapse time (t_{COLLAPSE}) was 120 ns. The net membrane displacement was 757 Å. At $t = 2$ μs, the voltage was changed back to 50 V. The time response of average membrane displacement crossed the static membrane displacement value of -67 Å at $t = 2.110$ μs. The snapback time (t_{SNAPBACK}) was 110 ns.

Average acoustic output pressure of the collapse-snapback operation (50–140 V) is depicted in Fig. 7(b). Acoustic output pressure was averaged over the plane 60 μm away from the cMUT surface. Collapse and snapback cycles of generated -1.05 MPa and 1.55 MPa peak acoustic output pressures, respectively. The peak acoustic output pressure magnitude generated in the collapse cycle was 70% of that generated in the snapback cycle.

TABLE III
PHYSICAL PARAMETERS OF THE 2-D CMUT USED IN EXPERIMENTS.

Length of the transducer, μm	1180
Width of the transducer, μm	280
Number of cells per element	4×52
Cell shape factor	Hexagon
Cell radius, μm	16
Electrode radius, μm	8
Electrode thickness, μm	0.3
Membrane thickness, μm	1.06
Gap thickness, μm	0.22
Insulating layer thickness, μm	0.3
Silicon substrate thickness, μm	500
Collapse voltage, V	130
Snapback voltage, V	110

The physical parameters of the cMUT used in the experiments are listed in Table III. The active area of the cMUT was 64% of the total 1180-μm $\times$ 280-μm transducer area, which consisted of four 2-D cMUT array elements connected together.

Transmit experiments were performed by measuring the pressure produced by the cMUT, using a calibrated hydrophone in the far field. The details of the experimental setup can be found in [9]. The measured voltage signal by the hydrophone was processed in the frequency domain with the hydrophone calibration, the attenuation, and the diffraction spectrums, and inverse Fourier was used to determine the pressure at the cMUT surface as a function of time.

Average acoustic pressures on the cMUT surface are depicted in Figs. 8(a)–(d). The cMUT was biased at 50 V, and was excited by a +70 V pulse for $t_P = 1$ μs in the conventional operation [Fig. 8(a)]. In the rising edge of the pulse, peak-to-peak pressure of 0.18 MPa was generated whereas the falling edge of the pulse produced 0.35 MPa peak-to-peak pressure. The pulse was increased to +80 V in the conventional operation [Fig. 8(b)]. In the

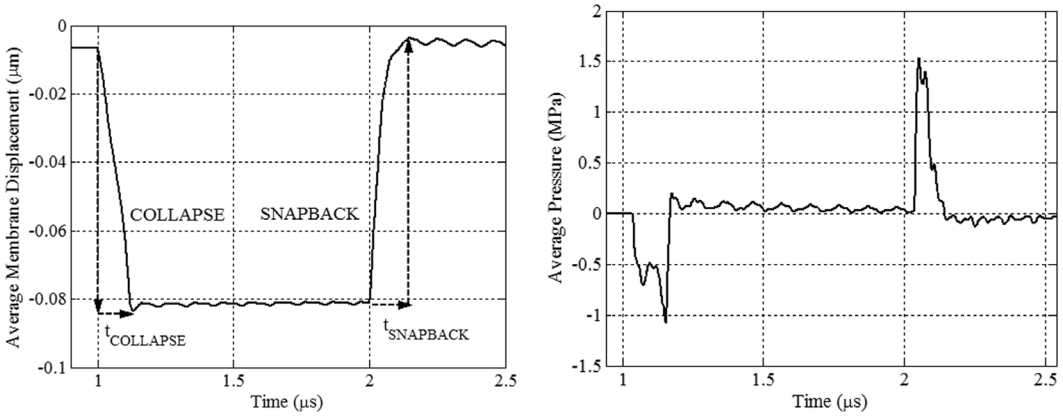

Fig. 7. 3-D dynamic finite element results for a 2-D square cMUT cell. Bias voltage is 50 V. $V_P = +90$ V is applied for $t_P = 1$ μs. (a) Average membrane displacement of the cMUT. (b) Average pressure of the cMUT.

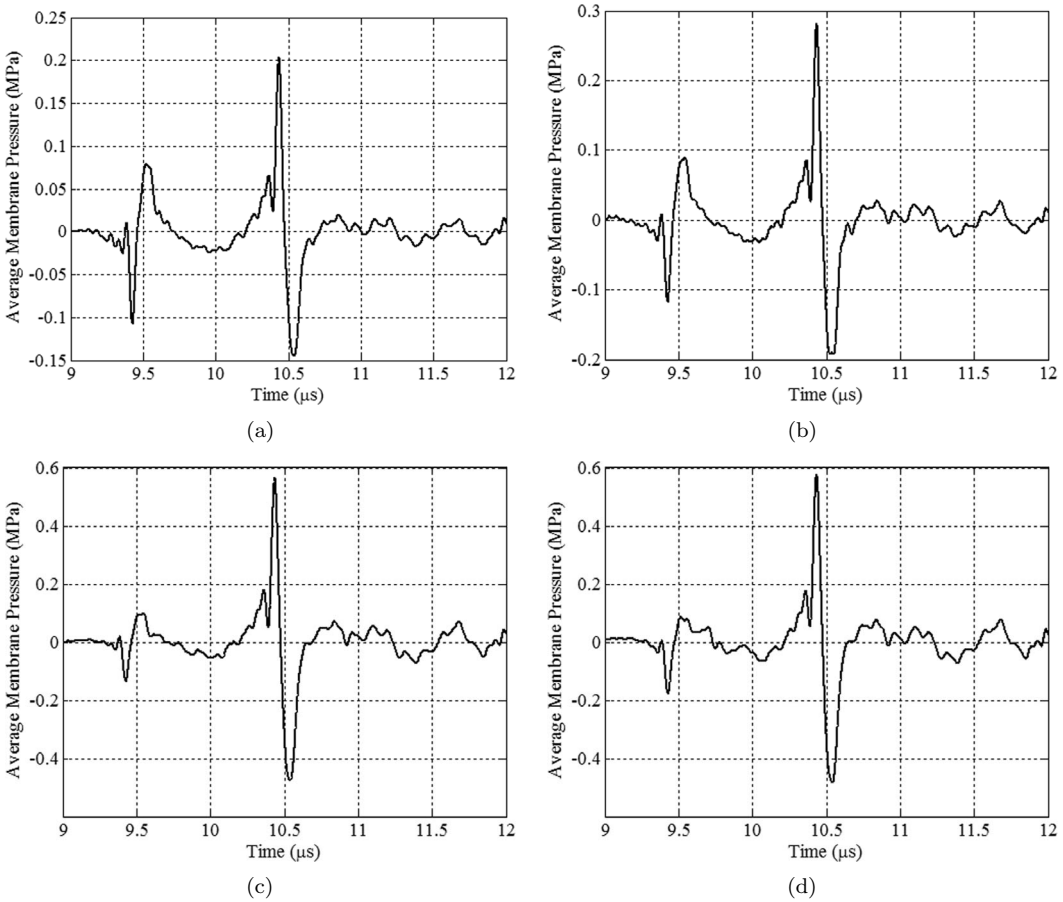

Fig. 8. Experimental results: Average membrane pressure. Bias voltage is 50 V. V_P is applied for $t_P = 1$ μs. (a) $V_P = 70$ V, conventional operation. (b) $V_P = 80$ V, conventional operation. (c) $V_P = 90$ V, collapse-snapback operation. (d) $V_P = 100$ V, collapse-snapback operation.

rising edge of the pulse, peak-to-peak pressure of 0.21 MPa was generated whereas the falling edge of the pulse produced 0.47 MPa peak-to-peak pressure. The pulse was increased to +90 V for the collapse-snapback operation [Fig. 8(c)]. In the collapsing cycle, peak-to-peak pressure of 0.23 MPa was generated whereas the snapback cycle produced 1.04 MPa peak-to-peak pressure. The pulse was further increased to +100 V in the collapse-snapback operation [Fig. 8(d)]. In the collapsing cycle, peak-to-peak pressure of 0.27 MPa was generated whereas the snapback cycle produced 1.06 MPa peak-to-peak pressure. Therefore, increasing the pulse in the collapse-snapback operation did not significantly influence the peak-to-peak pressure. However, transition from the conventional to collapse-snapback operation increased the peak-to-peak pressure of the snapback cycle from 0.47 MPa (+80 V pulse) to 1.04 MPa (+90 V pulse).

Average acoustic output pressures of the snapback cycle [Figs. 8(a)–(d)] were windowed from 10 μs to 11 μs and the frequency spectra of these pressures were calculated (Fig. 9). Regardless of the pulse amplitude, the center frequency of 4.2 MHz (4.1–4.3 MHz) with 95% (93–98%) fractional bandwidth was achieved for both conventional and collapse-snapback operations. Peak pressures of −12.6 dB (re. 1 MPa, +70 V pulse) and −9.8 dB (re. 1 MPa, +80 V pulse) in the conventional operation increased to −2.6 dB (re. 1 MPa, +90 V pulse) and −2.2 dB (re. 1 MPa, +100 V pulse) in the collapse-snapback operation.

The transition from the conventional to the collapse-snapback operation was investigated by unipolar [Figs. 10(a) and (b)] and bipolar [Figs. 10(c) and (d)] pulse excitations. The bias voltage was set to 70 V, and a unipolar pulse amplitude ($t_P = 1$ μs) was swept from 20 V to 80 V [Fig. 10(a)]. The above-mentioned peak-to-peak pressure of the snapback cycle was measured for the unipolar pulse amplitude. The peak-to-peak pressure increased linearly from 0.05 MPa at $V_P = 20$ V to 0.35 MPa at $V_P = 60$ V. When the pulse amplitude was changed between 60 V and 70 V, the rate of change of the peak-to-peak pressure increased significantly due to the collapse-snapback operation. The peak-to-peak pressure increased to 0.75 MPa at $V_P = 70$ V. Further increase of the pulse amplitude to 80 V did not change the peak-to-peak pressure (0.76 MPa). The peak-to-peak pressure per volt changed between 3 kPa/V ($V_P = 20$ V) and 6 kPa/V ($V_P = 60$ V) in the conventional operation [Fig. 10(b)]. The collapse-snapback operation increased the peak-to-peak pressure per volt to 11 kPa/V at $V_P = 70$ V. Increasing the pulse amplitude to 80 V reduced the peak-to-peak pressure per volt to 9.5 kPa/V. Therefore, the highest pressure per volt was achieved with $V_P = 70$ V at 70 V bias voltage. The transition from the conventional to the collapse-snapback operation happened at $V_P = 60$ V, which corresponded to 130 V (high) and 70 V (low) total applied voltages.

The bias voltage was then changed to 105 V, and a bipolar pulse ($t_P = 1$ μs) was applied [Fig. 10(c)]. The bipolar pulse amplitude was swept from 10 V (+5 V, −5 V) to 90 V (+45 V, −45 V). The peak-to-peak pressure increased linearly from 0.05 MPa at $V_P = 10$ V to 0.24 MPa at $V_P = 40$ V. When the pulse amplitude was changed between 40 V and 65 V, the collapse-snapback operation significantly increased the rate of change of the peak-to-peak pressure. The peak-to-peak pressure increased up to 0.7 MPa at $V_P = 65$ V. Further increase of the pulse amplitude to 90 V mildly increased the peak-to-peak pressure to 0.8 MPa. The peak-to-peak pressure per volt changed between 5 kPa/V ($V_P = 10$ V) and 6 kPa/V ($V_P = 40$ V) in the conventional operation [Fig. 10(d)]. The collapse-snapback operation increased the peak-to-peak pressure per volt up to 11 kPa/V at $V_P = 65$ V. Increasing the pulse amplitude to 90 V reduced the peak-to-peak pressure per volt to 9 kPa/V. Therefore, the highest pressure per volt was achieved with $V_P = 65$ V at 105 V bias voltage. The transition from the conventional to the collapse-snapback operation happened at $V_P = 40$ V, which corresponded to 125 V (high) and 85 V (low) total applied voltages.

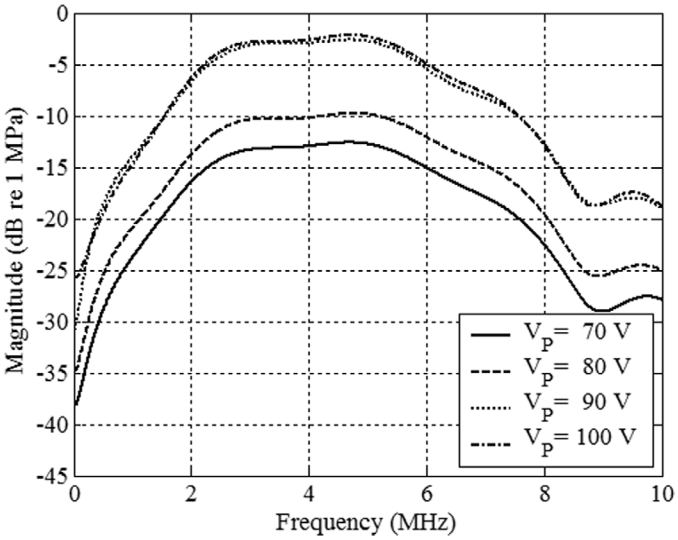

Fig. 9. Experimental results: Frequency spectrum of average membrane pressure. The solid and dashed lines represent pulse amplitudes of 70 V and 80 V in the conventional operation, respectively. The dotted and the dash-dotted lines represent pulse amplitudes of 90 V and 100 V in the collapse-snapback operation, respectively.

Finally, the unipolar pulse ($t_P = 1$ μs) with constant amplitude ($V_P = 100$ V) was applied as the bias voltage was swept from 20 V to 50 V [Fig. 10(e)]. The peak-to-peak pressure increased linearly from 0.25 MPa at $V_{BIAS} = 20$ V to 0.42 MPa at $V_{BIAS} = 35$ V. When the bias voltage was changed between 35 V and 47 V, the collapse-snapback operation significantly increased the rate of change of the peak-to-peak pressure. The peak-to-peak pressure increased up to 0.9 MPa at $V_{BIAS} = 47$ V. Further increase of the bias voltage (50 V) did not change the peak-to-peak pressure (0.9 MPa). The peak-to-peak pressure per volt changed between 2.5 kPa/V ($V_{BIAS} = 20$ V) and 4.2 kPa/V ($V_{BIAS} = 35$ V) in the conventional operation [Fig. 10(f)]. The collapse-snapback operation increased the peak-to-peak pressure per volt up to 9 kPa/V at $V_{BIAS} = 47$ V. The transition from the conventional to the collapse-snapback operation happened at

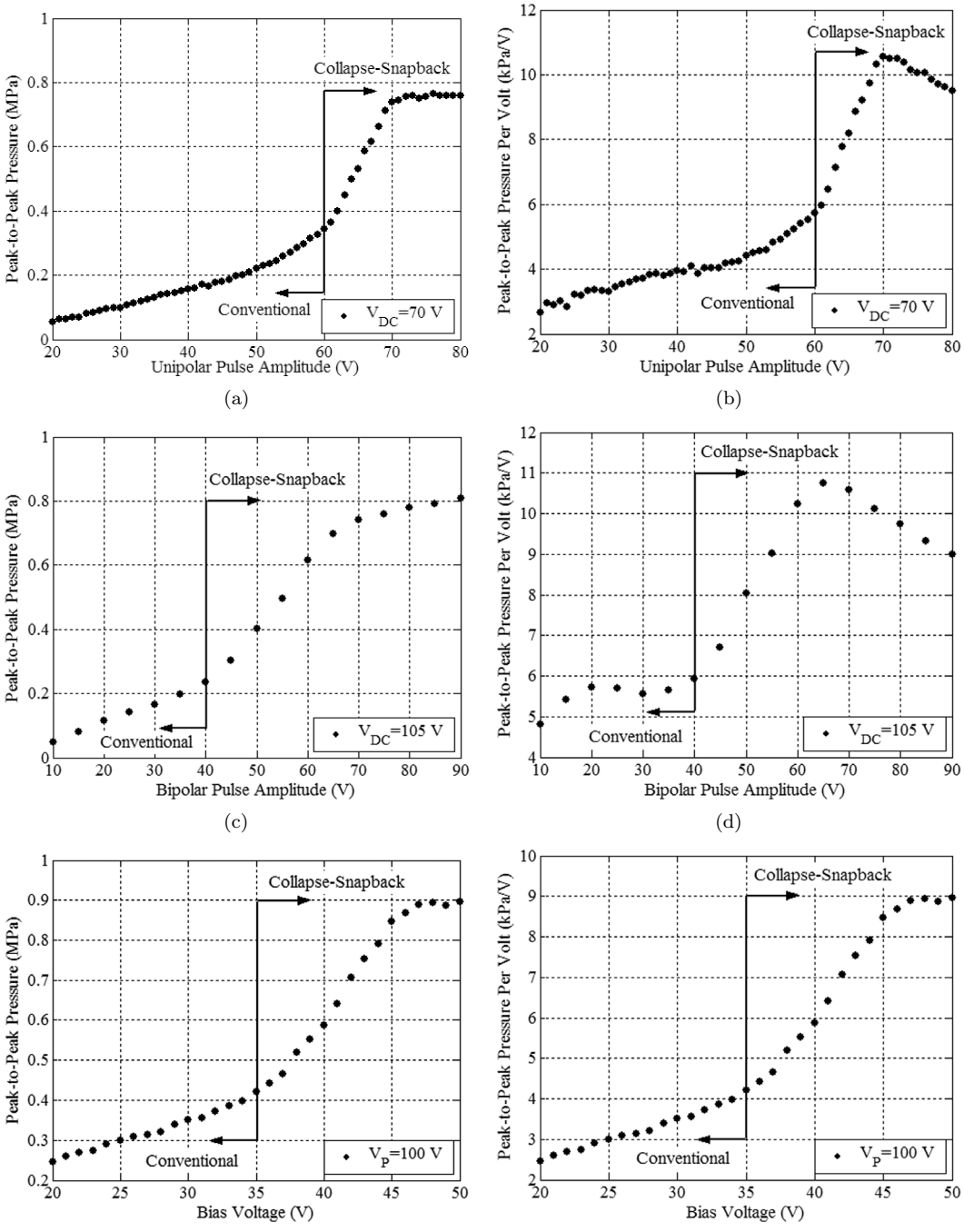

Fig. 10. Experimental results: Conventional and collapse-snapback operations, $t_P = 1$ μs. (a) Peak-to-peak pressure vs. unipolar pulse amplitude curve of the cMUT, $V_{DC} = 70$ V. (b) Peak-to-peak pressure per volt vs. unipolar pulse amplitude curve of the cMUT, $V_{DC} = 70$ V. (c) Peak-to-peak pressure vs. bipolar pulse amplitude curve of the cMUT, $V_{DC} = 105$ V. (d) Peak-to-peak pressure per volt vs. bipolar pulse amplitude curve of the cMUT, $V_{DC} = 105$ V. (e) Peak-to-peak pressure vs. bias voltage curve of the cMUT, $V_P = 100$ V. (f) Peak-to-peak pressure per volt vs. bias voltage curve of the cMUT, $V_P = 100$ V.

V_{BIAS} = 35 V, which corresponded to 135 V (high) and 35 V (low) total applied voltages.

IV. Discussion

In the static finite element calculations, a circular cMUT cell was modeled to investigate the influence of electrode parameters (r_e, d_e, t_e) on collapse and snapback voltages (Fig. 1). Thick silicon substrate (∼500 μm), used in actual transducers, had insignificant effect on the membrane deflections toward the insulation layer. Therefore, the substrate was modeled with a 1-μm-thick layer fixed on the bottom surface, reducing the computational cost of the analysis. The computational cost usually increased proportional to the model size (the number of elements used in the model). The average mesh size used in the model was 0.25 μm, which was optimal for accurate calculation of electrostatic and contact forces with a moderate computational cost. The nonlinear contact analysis required defining the surfaces that would contact each other. The contact surfaces were defined both on the bottom surface of the membrane and slightly above the insulation layer. The offset from the insulation layer was included to re-mesh the gap when the structure was collapsed. Re-meshing the gap was essential in the electrostatic analysis to determine the electrostatic forces accurately. However, the offset (5% of the gap) limited the maximum peak membrane displacement to 95% of the gap in collapse [Fig. 2(a)]. Therefore, electrostatic forces, which were inversely proportional to the square of the effective separation between the electrodes, were reduced by the offset. The snapback voltage was approximately 5–10% larger in the finite element calculations with the offset than without the offset. The collapse voltage was not affected by the offset, but was slightly dependent on the silicon nitride post, which was 1 μm thick in the x-direction. The collapse voltages were 5–8% smaller in this model than in models with thicker posts.

Atmospheric pressure and residual stress in the membrane were not included in the static analysis. Influence of air pressure on the membrane can be included later by adjusting the net gap, taking into account the atmospheric deflection. However, the atmospheric deflection should be only a small fraction of the gap, to avoid large induced membrane stresses resulting in a stiffer response. Wafer-bonded cMUT membranes have very low residual stress [25]. Surface micromachined cMUTs have considerable residual stress in the silicon nitride membrane [4]. However, the residual stress was neglected to better observe the influence of electrode parameters on the collapse and snapback voltages of the cMUT.

The collapse-snapback operation of the cMUT presented interesting results. Membrane displacements of conventional, collapsed, and collapse-snapback operations are compared in Fig. 2(b). The collapse and snapback of the membrane clearly contributed significant average displacement, which was not possible in conventional and collapsed operations. This paper focused on utilizing the large membrane displacement in actual practice.

The displacement per volt vs. electrode radius relationship suggested using electrodes with $r'_e > 0.6$ and $d_e \sim 0.2$ μm for better performance [Figs. 3(b) and (d)]. Displacement per cycle was larger for the electrode position $d_e = 0$ μm than for $d_e = 1$ μm [Figs. 3(a) and (c)]. Displacement per cycle for thicker membranes was larger despite the reduction of displacement per volt because collapse and snapback voltages were farther apart for thicker membranes.

The collapse and snapback voltages were calculated for electrode parameters such as radius, thickness and position [Figs. 4(a)–(d) and 5(a)–(b)]. These results can be used to design a cMUT with specific collapse and snapback voltages by modifying the electrode parameters. The performance of the cMUT (displacement per cycle) can be evaluated using Figs. 3(a)–(d).

Static and dynamic finite element calculations were used in the design of the cMUT given in Table II [Figs. 6(a) and (b) and 7(a) and (b)]. The insulation layer was 0.3 μm thick for reliable collapse-snapback operation. The collapse and snapback voltages were 130 V and 110 V, respectively [Fig. 6(a)]. Inclusion of the atmospheric pressure slightly reduced the collapse voltage (125 V) and did not change the snapback voltage (110 V) for this design. The average membrane displacement at 140 V was 0.07 μm in the static calculations [Fig. 6(b)] and 0.08 μm in the dynamic calculations [Fig. 7(a)]. This difference was due to the offset (5% of the gap) in the static model. The dynamic finite element calculations accurately determined the membrane displacement in collapse [Fig. 7(a)]. The snapback voltage was approximately 100 V with no offset in the model.

Displacement per cycle was calculated as 450 Å in the static FEM between collapse and snapback voltages [Fig. 6(b)]. In the dynamic FEM, the collapse and snapback times were calculated as 120 ns and 110 ns between 50 V and 140 V, respectively [Fig. 7(a)]. Therefore, the cMUT made full swing if the frequency of the pulse was lower than 4 MHz. One-MPa and 1.5-MPa acoustic pressures were generated on the cMUT surface in the collapse and snapback cycles, respectively [Fig. 7(b)]. The dynamic response of the cMUT was sufficient for collapse-snapback operation at a center frequency of 4 MHz. In the dynamic finite element calculations, an infinite cMUT array composed of identical cMUT cells was modeled, and accurately predicted the performance of a sufficiently large array [22].

An important contribution of this paper was the experimental results of the cMUT in collapse-snapback operation. The physical parameters of the 2-D cMUT array element used in the experiments are given in Table III. Since the cMUT was fabricated by the wafer-bonding technique, the silicon membrane was highly conductive, causing the applied voltage on the electrode to appear on the bottom of the entire membrane [25]. This assumption used in both static and dynamic finite element calculations was verified by the measurements performed on the cMUT.

The conventional and collapse-snapback operations are compared in Figs. 8(a)–(d). Conventional operation of the cMUT, biased at 50 V, produced 0.35 MPa and 0.47 MPa

in the falling edge of the pulse for +70 V and +80 V unipolar pulse excitations, respectively [Figs. 8(a) and (b)]. However, the collapse-snapback operation of the cMUT produced 1.04 MPa and 1.06 MPa in the falling edge of the pulse for +90 V and +100 V pulse excitations, respectively [Figs. 8(c) and (d)]. Therefore, the collapse-snapback operation increased the total acoustic output pressure as predicted earlier by the static FEM results.

The frequency spectra of the average membrane pressures generated by conventional (+70 V and +80 V) and collapse-snapback (+90 V and +100 V) operations are depicted in Fig. 9. The capacity of the collapse-snapback operation to produce superior output pressure is clearly seen during the transition between the operation regimes. The center frequency (4.2 MHz) and the fractional bandwidth (95%) did not change significantly between the conventional and collapse-snapback operation regimes. Therefore, the collapse-snapback operation offered the advantage of higher output pressure without degradation in the fractional bandwidth or shift in the center frequency. In the collapse-snapback operation, the change of pulse amplitude from +90 V to +100 V did not significantly improve the total acoustic output pressure. Thus, the design of cMUTs with specific collapse and snapback voltages to achieve the intended displacement per cycle was essential for the collapse-snapback operation, and made the static FEM-based optimization an integral part of the design process.

The transition between conventional and collapse-snapback operations is depicted in Figs. 10(a)–(f). The limited acoustic output pressure of the conventional operation (0.4 MPa) was almost doubled in the collapse-snapback operation (0.76 MPa) [Fig. 10(a)]. The transition occurred at $V_P = 60$ V for $V_{BIAS} = 70$ V. The collapse-snapback operation increased the peak-to-peak pressure per volt to 11 kPa/V at $V_P = 70$ V and $V_{BIAS} = 70$ V [Fig. 10(b)]. Similar results were achieved by bipolar pulse excitation.

Sweeping the bias voltage with +100 V unipolar pulse, the maximum peak-to-peak pressure of 0.9 MPa was achieved for a bias voltage of 50 V. This pressure was previously measured as 1.06 MPa [Fig. 8(d)]. Therefore, misalignment of the hydrophone and the cMUT surfaces was a possible cause of the 15% discrepancy. Another cause was the center-frequency variation at around 4 MHz. In this measurement, the hydrophone calibration data at 4 MHz were used to determine the pressure from the measured voltage signal. However, the center frequency was as large as 4.3 MHz in some cases (Fig. 9).

An important difference between the experimental and simulation results was observed: the step response of the cMUT generated one-sided pressure [Fig. 7(b)] in the simulations and two-sided pressure [Figs. 8(c) and (d)] in the experiments. The symmetry between the cells in the infinite transducer was a central assumption in the dynamic FEM calculations, and resulted in an overdamped dynamic response. However, the cMUT used in the experiment had a finite size (1180 μm × 280 μm). Therefore, the strictly enforced symmetry condition of the calculations was only weakly present, resulting in less damped response. Finite element calculations of a finite-size cMUT array ($n \times n$ cells, $n \sim 5$) is required for a better understanding of this difference. This modeling is currently under development.

Dynamic FEM calculations predicted higher acoustic output pressure in both the falling (1.5 MPa) and the rising (−1 MPa) edge of the pulse in the collapse-snapback operation [Fig. 7(b)]. However, in the experiments, the collapse-snapback operation did not significantly increase the acoustic pressure achieved in the collapsing cycle (0.18 MPa (+70 V), 0.21 MPa (+80 V), 0.23 MPa (+90 V), and 0.27 MPa (+100 V)). This odd behavior, not predicted by the calculations, was due to the above-mentioned finite size of the transducer. The weakly present symmetry among the cMUT cells caused double-sided pressure response. The symmetry also varied with the relative positions of the cells (close to the edge or close to the center), and caused nonuniform acoustic loading. The loading difference on the cMUT cells, depending on their relative position on the transducer area, introduced phase delay between the cells in the center and the cells at the edge. Out-of-phase response of the cMUT cells, combined with the double-sided pressure response, cancelled significant acoustic output pressure. The phase difference was more dominant in the rising than in the falling edge of the pulse. The dynamics were influenced primarily by the restoring force of the membrane for the falling edge of the pulse. However, both the electrostatic and the membrane restoring forces were present in the rising edge of the pulse. The strong dependence of electrostatic force on the electrode displacements introduced more phase delay in the rising edge of the pulse. The nature of the phase delay and its overall effect in the acoustic pressure may become clearer with a finite element analysis of a finite-size transducer in the future.

V. Conclusions

We presented the collapse-snapback operation of the cMUT for high-power transmission. The collapse-snapback operation utilizes a larger range of membrane deflection profiles (both collapsed and released membrane profiles) and generates higher acoustic output pressures than the conventional operation. The static finite element calculations were performed to design cMUTs with specific collapse and snapback voltages by changing the electrode parameters (radius (r_e), position (d_e), and thickness (t_e)). These designs were refined for optimum average displacement per cycle. An electrode radius greater than 60% of the membrane radius significantly improved the displacement per volt. Moderately thick membranes ($t_e \sim 0.2$ μm) were preferred, as thicker membranes reduced the displacement per volt. Dynamic finite element calculations of an infinite cMUT array on the substrate loaded with acoustic fluid medium were performed to determine the dynamic response of the cMUT. The transmit experiments were performed on the 2-D cMUT array using a calibrated hy-

drophone. Taking into account attenuation and diffraction losses, the pressure on the cMUT surface was extracted. The cMUT generated 0.47 MPa (6 kPa/V) and 1.04 MPa (11 kPa/V) in the conventional and collapse-snapback operations, respectively. Therefore, collapse-snapback operation of the cMUTs was superior for high-power transmission.

Acknowledgment

The authors thank Mr. Can Bayram from Bilkent University for developing the ultrasonic field analysis tool using LABVIEW to control the main components of the experimental setup (the UNIDEX positioning system, voltage supplies, amplifier, and oscilloscope), Dr. Wayne L. Mindle from Livermore Software Technology Corporation (LSTC) for providing technical assistance in LS-DYNA and providing the object files for user-defined loading implementation, Dr. Khanh Bui from LSTC for providing useful information about the coupled-field analysis using LS-DYNA, Dr. Morten Rikard Jensen from LSTC for providing technical support for full restart implementation in LS-DYNA, and Dr. Scott Rodamaker from MCR Associates, Inc. for providing technical support in ANSYS and ANSYS/LS-DYNA.

References

[1] M. I. Haller and B. T. Khuri-Yakub, "A surface micromachined electrostatic ultrasonic air transducer," in *Proc. IEEE Ultrason. Symp.*, 1994, pp. 1241–1244.

[2] H. T. Soh, I. Ladabaum, A. Atalar, C. F. Quate, and B. T. Khuri-Yakub, "Silicon micromachined ultrasonic immersion transducers," *Appl. Phys. Lett.*, vol. 69, pp. 3674–3676, Dec. 1996.

[3] P. C. Eccardt, K. Niederer, and B. Fischer, "Micromachined transducers for ultrasound applications," in *Proc. IEEE Ultrason. Symp.*, 1997, pp. 1609–1618.

[4] I. Ladabaum, X. Jin, H. T. Soh, A. Atalar, and B. T. Khuri-Yakub, "Surface micromachined capacitive ultrasonic transducers," *IEEE Trans. Ultrason., Ferroelect., Freq. Contr.*, vol. 45, no. 3, pp. 678–690, May 1998.

[5] Ö. Oralkan, A. S. Ergun, C. H. Cheng, J. A. Johnson, M. Karaman, T. H. Lee, and B. T. Khuri-Yakub, "Volumetric ultrasound imaging using 2-D cMUT arrays," *IEEE Trans. Ultrason., Ferroelect., Freq. Contr.*, vol. 50, no. 11, pp. 1581–1594, Nov. 2003.

[6] S. W. Smith, H. G. Pavy, Jr., and O. T. von Ramm, "High-speed ultrasound volumetric imaging system—Part I: Transducer design and beam steering," *IEEE Trans. Ultrason., Ferroelect., Freq. Contr.*, vol. 38, pp. 100–108, Mar. 1991.

[7] O. T. von Ramm, S. W. Smith, and H. G. Pavy, Jr., "High-speed ultrasound volumetric imaging system—Part II: Parallel processing and image display," *IEEE Trans. Ultrason., Ferroelect., Freq. Contr.*, vol. 38, pp. 109–115, Mar. 1991.

[8] A. Bozkurt, A. Atalar, and B. T. Khuri-Yakub, "Theory and analysis of electrode size optimization for capacitive microfabricated ultrasonic transducers," *IEEE Trans. Ultrason., Ferroelect., Freq. Contr.*, vol. 46, no. 6, pp. 1364–1374, Nov. 1999.

[9] Ö. Oralkan, X. Jin, F. L. Degertekin, and B. T. Khuri-Yakub, "Simulation and experimental characterization of a 2-D capacitive micromachined ultrasonic transducer array element," *IEEE Trans. Ultrason., Ferroelect., Freq. Contr.*, vol. 46, no. 6, pp. 1337–1340, Nov. 1999.

[10] M. Kaltenbacher, H. Landes, K. Niederer, and R. Lerch, "3D simulation of controlled micromachined capacitive ultrasound transducers," in *Proc. IEEE Ultrason. Symp.*, 1999, pp. 1155–1158.

[11] K. Niederer, P. C. Eccardt, H. Meixner, and R. Lerch, "Micromachined transducer design for minimized generation of surface waves," in *Proc. IEEE Ultrason. Symp.*, 1999, pp. 1137–1139.

[12] G. Wojcik, J. Mould, P. Reynolds, A. Fitzgerald, P. Wagner, and I. Ladabaum, "Time-domain models of MUT array cross-talk in silicon substrates," in *Proc. IEEE Ultrason. Symp.*, 2000, pp. 909–914.

[13] I. Ladabaum, P. Wagner, C. Zanelli, J. Mould, P. Reynolds, and G. Wojcik, "Silicon substrate ringing in microfabricated ultrasonic transducers," in *Proc. IEEE Ultrason. Symp.*, 2000, pp. 943–946.

[14] E. Zhelezina, M. Kaltenbacher, and R. Lerch, "Numerical simulation of acoustic wave propagation by a time and space adaptive finite element method," in *Proc. IEEE Ultrason. Symp.*, 2002, pp. 1213–1216.

[15] Y. Roh and B. T. Khuri-Yakub, "Finite element analysis of underwater capacitor micromachined ultrasonic transducers," *IEEE Trans. Ultrason., Ferroelect., Freq. Contr.*, vol. 49, no. 3, pp. 293–298, Mar. 2002.

[16] M. Kaltenbacher, H. Landes, S. Reitzinger, and R. Peipp, "3-D simulation of electrostatic-mechanical transducers using algebraic multigrid," *IEEE Trans. Magn.*, vol. 38, no. 2, pp. 985–988, Mar. 2002.

[17] A. Lohfink, P. C. Eccardt, W. Benecke, and H. Meixner, "Derivation of a 1D cMUT model from FEM results for linear and nonlinear equivalent circuit simulation," in *Proc. IEEE Ultrason. Symp.*, 2003, pp. 465–468.

[18] J. Fraser and P. Reynolds, "Finite-element method for determination of electromechanical coupling coefficient for piezoelectric and capacitive micromachined ultrasonic transducers," in *Joint 140th meeting of ASA/NOISE-CON*, 2000.

[19] B. Bayram, E. Hæggström, G. G. Yaralioglu, and B. T. Khuri-Yakub, "A new regime for operating capacitive micromachined ultrasonic transducers," *IEEE Trans. Ultrason., Ferroelect., Freq. Contr.*, vol. 50, no. 9, pp. 1184–1190, Sep. 2003.

[20] Y. Huang, B. Bayram, A. S. Ergun, E. Hæggström, C. H. Cheng, and B. T. Khuri-Yakub, "Collapsed region operation of capacitive micromachined ultrasonic transducers based on wafer-bonding technique," in *Proc. IEEE Ultrason. Symp.*, vol. 2, 2003, pp. 1161–1164.

[21] B. Bayram, E. Hæggström, G. G. Yaralioglu, and B. T. Khuri-Yakub, "Dynamic analysis of cMUTs in different regimes of operation," *Proc. IEEE Ultrason. Symp.*, vol. 1, 2003, pp. 481–484.

[22] B. Bayram, G. G. Yaralioglu, A. S. Ergun, Ö. Oralkan, and B. T. Khuri-Yakub, "Dynamic analysis of capacitive micromachined ultrasonic transducers," *IEEE Trans. Ultrason., Ferroelect., Freq. Contr.*, submitted for publication.

[23] X. C. Jin, I. Ladabaum, and B. T. Khuri-Yakub, "The microfabrication of capacitive ultrasonic transducers," *IEEE/ASME J. Microelectromech. Syst.*, vol. 7, pp. 295–302, Sep. 1998.

[24] X. C. Jin, I. Ladabaum, F. L. Degertekin, S. Calmes, and B. T. Khuri-Yakub, "Fabrication and characterization of surface micromachined capacitive ultrasonic immersion transducers," *IEEE/ASME J. Microelectromech. Syst.*, vol. 8, pp. 100–114, Mar. 1999.

[25] Y. Huang, A. S. Ergun, E. Hæggström, M. H. Badi, and B. T. Khuri-Yakub, "Fabricating capacitive micromachined ultrasonic transducers with wafer-bonding technology," *IEEE J. Microelectromech. Syst.*, vol. 12, no. 2, pp. 128–137, Apr. 2003.

[26] ANSYS 5.7, Ansys Inc., Southpointe, 275 Technology Drive, Canonsburg, PA 15301, USA.

[27] LS-DYNA 970, Livermore Software Technology Corporation, Livermore, CA 94551, USA.

Baris Bayram was born in Izmir, Turkey. He received the B.S. degree in 2000 from Bilkent University, Turkey, the M.S. degree in 2002 from Stanford University, both in electrical engineering. He is currently a Ph.D. candidate in electrical engineering at the E. L. Ginzton Laboratory of Stanford University. His current research interests include the accurate modeling of capacitive micromachined ultrasonic transducers (cMUTs) using static and dynamic FEM. He particularly investigates

the nonlinear operation regimes (collapsed and collapse-snapback) of cMUTs for high performance. He is a member of the IEEE.

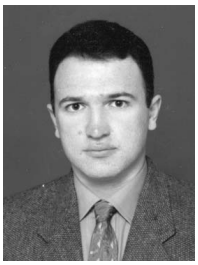

Ömer Oralkan (S'93) was born in Izmit, Turkey, in 1973. He received a B.S. degree from Bilkent University, Ankara, Turkey, in 1995, an M.S. degree from Clemson University, Clemson, SC, in 1997, and a Ph.D. degree from Stanford University, Stanford, CA, in 2004, all in electrical engineering.

From 1995 to 1996, he was a hardware and network engineer at Bilkent University Computer Center, Ankara, Turkey. In the summer of 1997, he worked as a process engineer at the National Semiconductor Research Laboratories, Santa Clara, CA. Currently, he is an engineering research associate at the Edward L. Ginzton Laboratory at Stanford University. His past and present research interests include analog and digital circuit design, micromachined sensors and actuators, and semiconductor device physics and fabrication. His current research focuses on the design and implementation of integrated ultrasonic imaging systems.

He is a co-recipient of the Best Paper Award presented at the IEEE International Symposium on the Physical and Failure Analysis (IPFA). He also received the 2002 Outstanding Paper Award of the IEEE Ultrasonics, Ferroelectrics, and Frequency Control Society. Dr. Oralkan is a member of the IEEE.

Arif Sanli Ergun (S'91, M'99) was born in Ankara, Turkey, in 1969. He received his B.Sc., M.Sc., and Ph.D. degrees in 1991, 1994, and 1999, respectively, all in electrical and electronics engineering from Bilkent University, Turkey. He is now at the E. L. Ginzton Laboratory, Stanford University, as an engineering research associate. His main research interests are acoustics, ultrasound, microelectromechanical systems (MEMS), and microwave electronics.

Edward Hæggström is a visiting scholar at the Ginzton Laboratory (Khuri-Yakub group), Stanford University, CA, on leave from his position as assistant professor at the Department of Physics at the University of Helsinki. He received his D.Sc. degree in 1998 in applied physics from the University of Helsinki, Finland, and an MBA degree in innovation management from the Helsinki University of Technology in 2001. His principal research interests are within ultrasonic characterization of biological samples.

Goksen Goksenin Yaralioglu (S'92, M'99) was born in Akhisar, Turkey, on May 13, 1970. He received his B.S., M.S., and Ph.D. degrees from Bilkent University, Turkey, in 1992, 1994, and 1999, respectively, all in electrical engineering. He is now working as an engineering research associate in E. L. Ginzton Laboratory, Stanford University. His current research interests include design, modeling and applications of micromachined ultrasonic transducers, and atomic force microscopy at ultrasonic frequencies.

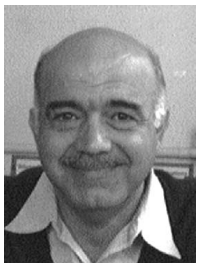

Butrus T. Khuri-Yakub (S'70, S'73, M'76, SM'87, F'95) was born in Beirut, Lebanon. He received the B.S. degree in 1970 from the American University of Beirut, the M.S. degree in 1972 from Dartmouth College, and the Ph.D. degree in 1975 from Stanford University, all in electrical engineering. He joined the research staff at the E. L. Ginzton Laboratory of Stanford University in 1976 as a research associate. He was promoted to senior research associate in 1978, and to a Professor of Electrical Engineering (Research) in 1982. He has served on many university committees in the School of Engineering and the Department of Electrical Engineering.

Presently, he is the Deputy Director of the E. L. Ginzton Laboratory, and the associate chairman for graduate admissions in the electrical engineering department at Stanford. Professor Khuri-Yakub has been teaching both at the graduate and undergraduate levels for over 20 years, and his current research interests include in situ acoustic sensors (temperature, film thickness, resist cure, etc.) for monitoring and control of integrated circuits manufacturing processes, micromachining silicon to make acoustic materials and devices such as airborne and water immersion ultrasonic transducers and arrays, and fluid ejectors, and in the field of ultrasonic nondestructive evaluation and acoustic imaging and microscopy.

Professor Khuri-Yakub is a fellow of the IEEE, a senior member of the Acoustical Society of America, and a member of Tau Beta Pi. He is associate editor of Research in Nondestructive Evaluation, a Journal of the American Society for Nondestructive Testing. Professor Khuri-Yakub has authored over 400 publications and has been principal inventor or co-inventor of 60 issued patents. He received the Stanford University School of Engineering Distinguished Advisor Award, June 1987, and the Medal of the City of Bordeaux for contributions to NDE, 1983.